2D Heat and Mass Transfer Modeling of Methane Steam Reforming for Hydrogen Production in a Compact Reformer

Meng Ni

Building Energy Research Group, Department of Building and Real Estate,

The Hong Kong Polytechnic University, Hung Hom, Kowloon, Hong Kong, P.R. China

Abstract:

Compact reformers (CRs) are promising devices for efficient fuel processing. In CRs, a thin solid plate is sandwiched between two catalyst layers to enable efficient heat transfer from combustion duct to the reforming duct for fuel processing. In this study, a 2D heat and mass transfer model is developed to investigate the fundamental transport phenomenon and chemical reaction kinetics in a CR for hydrogen production by methane steam reforming (MSR). Both MSR reaction and water gas shift reaction (WGSR) are considered in the numerical model. Parametric simulations are performed to examine the effects of various structural/operating parameters, such as porosity, permeability, gas velocity, temperature, and rate of heat supply on the reformer performance. It is found that the reaction rates of MSR and WGSR are the highest at the inlet but decrease significantly along the reformer. Increasing the operating temperature raises the reaction rates at the inlet but shows very small influence in the downstream. For comparison, increasing the rate of heat supply raises the reaction rates in the downstream due to increased temperature. A high gas velocity and permeability facilitates gas transport in the porous structure thus enhances reaction rates in the downstream of the reformer.

Keywords: Compact reformer; Fuel processing; Porous media; Heat and mass transfer; Hydrogen production

---

* Corresponding author. Tel: (852) 2766 4152; Fax: (852) 2764 5131;
Email: meng.ni@polyu.edu.hk (Meng Ni)

1. Introduction

Hydrogen is an ideal energy carrier to support sustainable energy development [1]. Using a fuel cell, hydrogen can be efficiently converted into electricity with water as the by-product. To make the hydrogen energy and fuel cell commercially feasible, it is critical to produce hydrogen efficiently and economically at a large scale.

In the long term, hydrogen can be produced in a clean way by solar thermochemical water splitting, photocatalytic water splitting or water electrolysis driven by solar cells/wind turbines [2,3]. However, the present energy efficiencies of both thermochemical and photocatalytic hydrogen production methods are too low to be economically viable (i.e. efficiency for photocatalytic hydrogen production is usually less than 1% [2]). Water electrolytic hydrogen production can be a promising technology for large scale hydrogen production but the cost is still high, due to the use of expensive catalyst, i.e. Pt. For comparison, steam reforming of hydrocarbon fuels (i.e. methane) is efficient and can be a feasible way for hydrogen production for the near term [4]. In general, hydrogen production from methane is based on one of the following processes: methane steam reforming (MSR), partial oxidation (POX), and autothermal reforming (ATR) [5]. MSR is the most common method for hydrogen production from methane at a large scale. In MSR reaction (Eq.1), methane molecules react with steam molecules to produce hydrogen and carbon monoxide in the catalyst layer of reformers. Meanwhile, steam can react with carbon monoxide to produce additional hydrogen and carbon dioxide (Eq. 2), which is called water gas shift reaction (WGSR).

$$CH_4 + H_2O \leftrightarrow CO + 3H_2 \quad (1)$$

$$CO + H_2O \leftrightarrow CO_2 + H_2 \quad (2)$$

WGSR is exothermic while MSR is highly endothermic. As the MSR reaction rate is usually higher than WGSR, heat is required for hydrogen production by MSR and WGSR. The heat supply can be achieved by using a compact reformer (CR). A typical CR consists of a solid thin

plate sandwiched between two catalyst layers, as can be seen from Figure 1 (adapted from [6]). The small thickness of the thin plate allows efficient heat transfer from the combustion duct to the fuel reforming duct to facilitate chemical reactions in the catalyst layer. High power density resulted from the compactness nature of the CRs makes them suitable for stationary and transportation applications [7,8]. Although some preliminary studies have been performed for CRs, there is insufficient numerical modeling on CRs for hydrogen production by methane steam reforming, especially on how the various parameters affect the reformer performance. It's still not very clear how the change in inlet temperature and rate of heat supply can influence the coupled transport and reaction kinetics in the reformer, which are important for optimization of the reformer operation conditions. In addition, the study in the literature considers pre-reformed methane gas consisting of CH_4, H_2O, CO, CO_2, and H_2 gas mixture at the inlet [6]. While it may be more appropriate to use CH_4/H_2O mixture as the feeding gas to the reformer.

In this paper, 2D numerical model is developed to simulate the performance of a CR for methane reforming. Different from the previous studies using pre-reformed gas mixtures at the inlet, the present study uses a CH_4/H_2O mixture at the reformer inlet. In real application, the steam to carbon ratio (SCR) is an important parameter as carbon deposition can occur at a low (i.e. less than 1) SCR [9]. As the present study do not consider the carbon deposition behavior in the reformer, a constant SCR of 2.0 is adopted. The effects of the reformer structural/operating parameters on the coupled transport and reaction phenomena are investigated and discussed in detail.

2. Model development

A 2D model is developed for hydrogen production from methane reforming in a CR. Heat from the combustion duct is supplied to the Ni-based (i.e. [10]) catalyst layer via the solid thin film

layer and it is specified as a boundary condition [6]. Without considering the 3D effect, the coupled transport and chemical reaction phenomena in the computational domain can be shown in Figure 2, including the solid plate, the reforming duct, and the porous catalyst layer. The 2D model consists of a chemical model and a CFD model. The chemical model is developed to calculate the rates of chemical reactions and corresponding reaction heats. The CFD model is used to simulate the heat and mass transfer phenomena in the CR.

2.1 Chemical model

In operation, methane-containing gas mixture (CH_4: 33%; H_2O: 67%) is supplied to the reforming duct. The gas species are then transported from the gas duct into the porous catalyst layer, where MSR reaction (Eq. 1) and WGSR (Eq. 2) take place. The formulas proposed by Haberman and Young [11] have been widely used for simulating the rates (mol.m^{-3}.s^{-1}) of MSR (R_{MSR}) and WGSR (R_{WGSR}), thus is adopted in the present study.

$$R_{MSR} = k_{rf}\left(P_{CH_4}P_{H_2O} - \frac{P_{CO}\left(P_{H_2}\right)^3}{K_{ps}}\right) \tag{3}$$

$$k_{rf} = 2395\exp\left(\frac{-231266}{RT}\right) \tag{4}$$

$$K_{pr} = 1.0267\times10^{10}\times\exp\left(-0.2513Z^4 + 0.3665Z^3 + 0.5810Z^2 - 27.134Z + 3.277\right) \tag{5}$$

$$R_{WGSR} = k_{sf}\left(P_{CO}P_{H_2O} - \frac{P_{CO_2}P_{H_2}}{K_{ps}}\right) \tag{6}$$

$$k_{sf} = 0.0171\exp\left(\frac{-103191}{RT}\right) \tag{7}$$

$$K_{ps} = \exp\left(-0.2935Z^3 + 0.6351Z^2 + 4.1788Z + 0.3169\right) \tag{8}$$

$$Z = \frac{1000}{T(K)} - 1 \tag{9}$$

where T is the temperature (K), R is the universal gas constant (8.3145 J.mol^{-1}K^{-1}). P is partial pressures of gas species (Pa).

The amount of heat generation from WGSR and heat consumption by MSR reaction can be calculated using corresponding enthalpy changes [12]. Assuming linear dependence on operating temperature between 600K and 1200K, the reaction heats (J.mol^{-1}) for MSR reaction and WGSR can be calculated as [13].

$$H_{MSR} = -\left(206205.5 + 19.5175T\right) \tag{10}$$

$$H_{WGSR} = 45063 - 10.28T \tag{11}$$

2.2. Computational Fluid Dynamics (CFD) model

Assuming local thermal equilibrium in the porous catalyst layer, the governing equations for mass conservation, momentum conservation, and energy conservation for the whole computational domain are summarized below [14].

$$\frac{\partial(\rho U)}{\partial x} + \frac{\partial(\rho V)}{\partial y} = 0 \tag{12}$$

$$\frac{\partial(\rho UU)}{\partial x} + \frac{\partial(\rho VU)}{\partial y} = -\frac{\partial P}{\partial x} + \frac{\partial}{\partial x}\left(\mu \frac{\partial U}{\partial x}\right) + \frac{\partial}{\partial y}\left(\mu \frac{\partial U}{\partial y}\right) + S_x \tag{13}$$

$$\frac{\partial(\rho UV)}{\partial x} + \frac{\partial(\rho VV)}{\partial y} = -\frac{\partial P}{\partial y} + \frac{\partial}{\partial x}\left(\mu \frac{\partial V}{\partial x}\right) + \frac{\partial}{\partial y}\left(\mu \frac{\partial V}{\partial y}\right) + S_y \tag{14}$$

$$\frac{\partial(\rho c_P UT)}{\partial x} + \frac{\partial(\rho c_P VT)}{\partial y} = \frac{\partial}{\partial x}\left(k \frac{\partial T}{\partial x}\right) + \frac{\partial}{\partial y}\left(k \frac{\partial T}{\partial y}\right) + S_T \tag{15}$$

$$\frac{\partial(\rho UY_i)}{\partial x} + \frac{\partial(\rho VY_i)}{\partial y} = \frac{\partial}{\partial x}\left(\rho D_{i,m}^{eff} \frac{\partial Y_i}{\partial x}\right) + \frac{\partial}{\partial y}\left(\rho D_{i,m}^{eff} \frac{\partial Y_i}{\partial y}\right) + S_{sp} \tag{16}$$

where U and V are the velocity components in x and y directions respectively; ρ and μ are the density and viscosity of the gas mixture; k is the thermal conductivity; c_p is the heat capacity; $D_{i,m}^{eff}$ is the effective diffusion coefficient of species i in gas mixture. Both ρ and μ depend on the local composition and temperature of the gas mixture, which is treated as an ideal gas. In the porous catalyst layer, effective heat conductivity and heat capacity are used and can be calculated as [15],

$$k = \varepsilon k_f + (1-\varepsilon) k_s \tag{17}$$

$$c_p = \varepsilon c_{p,f} + (1-\varepsilon) c_{p,s} \tag{18}$$

where ε is the porosity of the porous catalyst layer; k_f and k_s are the heat conductivity ($W.m^{-1}.K^{-1}$) of the fluid and solid, respectively; $c_{p,f}$ and $c_{p,s}$ are the heat capacity ($J.kg^{-1}.K^{-1}$) of the fluid and solid, respectively.

The mass fraction of species i (Y_i) can be related to the molar fraction (X_i) and molecular weight (M_i) of species i,

$$Y_i = X_i \left(\frac{M_i}{\sum_{i=1}^{N} X_i M_i} \right) \tag{19}$$

The density of the gas mixture ρ can be calculated as,

$$\rho = \frac{1}{\sum_{i=1}^{N} Y_i / \rho_i} \tag{20}$$

where ρ_i is the density of gas species i.

The viscosity of the gas mixture (μ) can be obtained by Wilke's method [16]

$$\mu = \sum_{i=1}^{n} \frac{y_i \mu_i}{\sum_{j=1}^{n} y_j \varphi_{ij}} \tag{21}$$

The value of φ_{ij} can be determined by Herning and Zipperer approximation as [16]

$$\varphi_{ij} = \sqrt{\frac{M_j}{M_i}} = \varphi_{ji}^{-1} \tag{22}$$

The effective diffusion coefficient of species *i* ($D_{i,m}^{eff}$) can be determined as [17]:

$$\frac{1}{D_{i,m}^{eff}} = \frac{\xi}{\varepsilon}\left(\frac{\sum_{j \neq i} \frac{X_j}{D_{ij}}}{1 - X_i} + \frac{3}{2r_p}\sqrt{\frac{\pi M_i}{8RT}} \right) \tag{23}$$

$$D_{ij} = \frac{0.0026T^{1.5}}{p\sqrt{\frac{2M_iM_j}{M_j + M_i}}\left(\frac{\sigma_i + \sigma_j}{2}\right)^2 \Omega_D} \tag{24}$$

$$\Omega_D = \frac{1.06036}{\left(\frac{k_bT}{\varepsilon_{i,j}}\right)^{0.1561}} + \frac{0.193}{\exp\left(0.47635\left(\frac{k_bT}{\varepsilon_{i,j}}\right)\right)} + \frac{1.03587}{\exp\left(1.52996\left(\frac{k_bT}{\varepsilon_{i,j}}\right)\right)} + \frac{1.76474}{3.89411\left(\frac{k_bT}{\varepsilon_{i,j}}\right)} \tag{25}$$

where ξ / ε is the ratio of tortuosity to porosity of porous catalyst layer; and r_p is the radius of pores. D_{ij} is the binary diffusion coefficient of species *i* and *j*. σ is the mean characteristic length of species and Ω_D is a dimensionless diffusion collision. k_b is the Boltzmann's constant ($1.38066\times10^{-23}\left(\text{J.K}^{-1}\right)$). The values of σ_i and $\varepsilon_{i,j}$ used in the present study are summarized in Table 1 [16].

The Darcy's law (Eq.26 and 27) is used as source terms in momentum equations (Eqs. (13) and (14)), so that the momentum equations are applicable for both the gas channels and the porous catalyst layers. A suitable permeability (B_g) is assigned to the porous catalyst layer and an infinitely large permeability is used for the reforming duct. The source term in energy equation (Eq. (15)) represents reaction heat from the chemical reactions can be calculated by Eq. (28). The source term in species equation (Eq. 16) represents the mass consumption/generation by MSR and WGSR reactions. Detailed descriptions of the source terms can be found in the previous publications [17].

$$S_x = -\frac{\mu U}{B_g} \tag{26}$$

$$S_y = -\frac{\mu V}{B_g} \tag{27}$$

$$S_T = R_{MSR} H_{MSR} + R_{WGSR} H_{WGSR} \tag{28}$$

2.3 Numerical scheme

The governing equations in the CFD model are solved with the finite volume method (FVM) [14]. As a real reformer stack consists of many identical single compact reformers, it is assumed that heat is supplied from the combustion channel (Fig. 1) and there is no heat transfer between compact reformers through the upper boundary ($y=y_M$). Therefore, adiabatic condition is applied to the upper boundary ($y = y_M$) while a constant heat flux is specified at the lower boundary ($y = 0$). The convection terms and diffusion terms are treated with the upwind difference scheme and central difference scheme, respectively. The velocity and pressure are linked with the SIMPLEC algorithm. The TDMA based alternative iteration scheme is employed to solve the discretized equations. The rates of chemical reactions and corresponding reaction heats obtained from the chemical model are used as source terms in the CFD model. Computation is repeated until convergence is achieved. The in-house code is written in FORTRAN.

3. Results and discussions

The chemical model and CFD model have been validated in the previous publications by comparing the modeling results with data from the literature [17]. The dimensions and typical simulation parameters are summarized in Table 2. The following sections focus on parametric simulations to analyze the effects of operating and structural parameters on the coupled transport

and reaction kinetics in CR. The effects of SCR and the catalyst nature on CR performance are not included but will be considered in future works.

3.1 Coupled transport and reaction in a compact reformer for hydrogen production

Figure 3 shows the distributions of MSR reaction rates, WGSR rates, temperature, velocity, gas composition (CH_4 and H_2 as examples) in the compact reformer at an inlet temperature of 1073K, inlet gas velocity of $3 m.s^{-1}$, and heat supply rate (from the solid plate) of $1 kW.m^{-2}$. The reaction rates for MSR and WGSR are the highest (25.4 and 14 $mol.m^{-3}.s^{-1}$ respectively) at the inlet and decrease considerably in the downstream of the reformer (Fig. 3a and 3b). The calculated reaction rates are well consistent with the experimental data from refs [18,19]. The high reaction rates near the inlet are mainly caused by high concentration of the reactants, especially the concentration of CH_4 (for MSR) and H_2O (for WGSR). In addition, the temperature is the highest at the inlet (Fig. 3c). The calculated reaction rates for MSR are in general higher than those for WGSR (Fig. 3a and 3b). As MSR reaction is endothermic while WGSR is exothermic, the temperature decreases from 1073K at the inlet to about 1007K at the outlet (Fig. 3c). Figure 3d shows the velocity contours profile (U/U_0) along the main flow stream. Similar to forced duct flow, velocity ratio (U/U_0) increases from zero near the wall to the highest in the core zone (Fig. 3d). The velocity in the catalyst layer is negligible due to small permeation (10^{-10} m^2) used in the simulation. The molar fraction of CH_4 is found to decrease along the CR flow channel (Fig. 3e), due to MSR reaction. A locally low molar fraction of CH_4 is also observed near the inlet in the catalyst layer (Fig. 3e). This is caused by high reaction rates of MSR and slow transport of CH_4 from the gas channel into the catalyst layer. For comparison, the molar fraction of H_2 increases along the CR gas flow stream (Fig. 3f). High molar fraction of H_2 is observed in the zones near the inlet and the outlet. The high molar fraction of H_2 near the inlet (in the catalyst layer) is mainly

caused by the locally high reaction rates of MSR and WGSR. The high molar fraction of H_2 near the outlet is caused by slow diffusion and thus accumulation of H_2 in the catalyst layer.

3.2. Effect of inlet temperature

To examine the effect of inlet temperature on CR performance, the distributions of reaction rates, temperature and gas composition at an inlet temperature of 1173K are shown in Figure 4. The reaction rates of MSR and WGSR are found to decrease along the main flow stream (Fig. 4a and 4b), but their values are significantly higher than those at 1073K (Fig. 3a and 3b). In addition, the reaction rates decrease more rapidly in the reformer than at 1073K. The high reaction rate of MSR causes the temperature to decrease rapidly along the main flow stream from 1173K at the inlet to about 1040K at the outlet (Fig. 4c). This temperature decrease is most pronounced near the inlet – decrease by about 100K within 3mm downstream from the inlet due to locally high rate of MSR reaction. As the reaction rates of MSR and WGSR are higher at 1173K than at 1073K, more CH_4 is consumed and more H_2 is produced, leading to larger gas composition variation in the reformer (Fig. 4d and 4e). For example, the molar fraction of CH_4 is decreased by about 13% from the inlet to the outlet while the molar fraction of H_2 is increased by about 20% at an inlet temperature of 1173K (Fig. 4d and 4e). In a word, increasing the inlet temperature increases the reaction rates, temperature gradient, and gas composition variation.

3.3. Effect of heat supply rate

The rate of heat supply is changed from $1kW.m^{-2}$ to $10kW.m^{-2}$ and $20kW.m^{-2}$ to investigate its effect on CR performance. As can be seen from Fig. 5, as the rate of heat supply is increased from $10kW.m^{-2}$ to $20kW.m^{-2}$, the reaction rates of both MSR and WGSR in the downstream are increased (Fig. 5a – 5d). For example, the reaction rate of MSR near the surface of the catalyst

layer at the outlet is about 40 $mol.m^{-3}.s^{-1}$ at a heat supply rate of $20kW.m^{-2}$ (Fig. 5b), while it's only about 20 $mol.m^{-3}.s^{-1}$ when the heat supply rate is $10kW.m^{-2}$ (Fig. 5a). In addition, the reaction rates near the catalyst surface is obviously higher than inside the catalyst layer, indicating the slow transport of gas species from the gas channel into the porous catalyst layer. The higher reaction rate in the downstream is due to higher temperature at a higher rate of heat supply (Fig. 5e and 5f). As can be seen from Fig. 5e, the temperature in CR decreases rapidly along the main flow stream due to high rate of MSR, followed by slight increase in the downstream at a heat supply rate of $10kW.m^{-2}$. At a higher heat supply rate ($20kW.m^{-2}$), the "cold spot" area is significantly reduced and the temperature in the downstream is even slightly higher than the inlet temperature (Fig. 5f). In addition, the lowest temperature in the reformer is increased to 1133K at a high heat supply rate (Fig. 5f).

3.4. Effect of inlet gas velocity and microstructure of the catalyst layer

In this section, the inlet gas velocity is increased from $3m.s^{-1}$ to $5m.s^{-1}$. The permeability and pore radius of the porous catalyst layer are increased from $2x10^{-10}$ m^2 to $2x10^{-8}$ m^2 and from 1μm to 5μm, respectively. The heat supply rate and inlet temperature are $10kW.m^{-2}$ and 1173K, respectively. As larger permeability and larger pore size facilitate gas permeation and diffusion into the porous catalyst layer, the reaction rates for MSR and WGSR in the downstream are propagated into the deeper catalyst layer (Fig. 6a and 6b), in comparison with Fig. 5a and 5c. Due to the slightly enhanced reaction rate in the downstream, the temperature in the reformer is slightly lower than at an inlet velocity of $3m.s^{-1}$ (Fig. 6c and 5e). The velocity contours profiles in the reformer again show similar pattern with forced duct flow (Fig. 6d). However, the core gas velocity is increased along the main flow stream to be about $1.55m.s^{-1}$. This velocity increase along the gas channel is mainly due to the fact that the total molar number of gas species increases

along the channel due to the MSR reaction (Eq. 1), which accelerates the gas flow. To examine the gas transport in the catalyst layer, the velocity contours are rescaled (Fig. 6e) and compared with the re-scaled velocity contours at an inlet velocity of $3 m.s^{-1}$ (Fig. 6f). As can be seen from Fig. 6e, large permeability enhances gas transport in the porous layer and the velocity in the whole catalyst layer is non-negligible. For comparison, at a smaller permeability, the gas velocity is non-negligible only in a very thin layer near the surface of the catalyst layer (Fig. 6f).

4. Conclusions

A two-dimensional heat and mass transfer model is developed to characterize the coupled transport and reaction phenomena in a compact reformer used for hydrogen production by methane steam reforming. Different from the previous studies using re-reformed gas mixtures, the CH_4/H_2O mixture is directly used at the inlet of CR in the present study. It's found that the reaction rates of MSR and WGSR are the highest at the inlet but decrease considerably along the reformer, due to large temperature drop along the main flow stream. Accordingly, locally low molar fraction of CH_4 and high molar fraction of H_2 are observed near the inlet. Increasing the inlet temperature from 1073K to 1173K increases the maximum reaction rates of MSR and WGSR but shows little effect on the reaction rates in the downstream. Moreover, raising the inlet temperature to 1173K enlarges the temperature drop to about 130K. For comparison, when the rate of heat supply is increased, the temperature in the downstream of the reformer is raised, leading to enhanced reaction rates of MSR and WGSR. It's also found that increasing the gas velocity and permeability facilitates the gas transport in the porous catalyst layer, which in turn enhances the reaction rates of MSR and WGSR in the downstream. The results of the present study provide good information on how the operating and structural parameters affect the coupled transport and reaction kinetics in CR, which are important for CR stack optimization.

Acknowledgements:

This research was supported by a grant (Project Number: PolyU 5238/11E) from Research Grant Council (RGC) of Hong Kong.

Symbols Used

B_g	[m^2]	Permeability of electrode
c_p	[kJ kg^{-1} K^{-1}]	Heat capactity
D_i^{eff}	[m^2 s^{-1}]	Effective diffusion coefficient of species *i*
$D_{i,k}$	[m^2 s^{-1}]	Knudsen diffusion coefficient of *i*
$D_{i,j}$	[m^2 s^{-1}]	Binary diffusion coefficient of *i* and *j*
F	[C mol^{-1}]	Faraday constant
k	[W m^{-1} K^{-1}]	Thermal conductivity
L	[m]	Thickness of electrolyte
M_i	[kg mol^{-1}]	Molecular weight of species *i*
P	[atm]	Operating pressure
R	[kJ mol^{-1} K^{-1}]	Universal gas constant
R_{MSR}	[mol m^{-3} s^{-1}]	Rate of methane steam reforming reaction
R_{WGSR}	[mol m^{-3} s^{-1}]	Rate of water gas shift reaction
r_p	[m]	Mean pore radius of electrode
S_m	[kg m^{-3} s^{-1}]	Source term in continuity equation
S_x, S_y	[kg m^{-2} s^{-2}]	Source terms in momentum equations
S_T	[W m^{-3}]	Source term in energy equation
S_{sp}	[kg m^{-3} s^{-1}]	Source term in species equations
ΔS	[kJ mol^{-1} K^{-1}]	Entropy change
T	[K]	Operating temperature
U	[m s^{-1}]	Velocity in x direction
U_0	[m s^{-1}]	Gas velocity at the inlet
V	[m s^{-1}]	Velocity in *y* direction
X_i	[-]	Molar fraction of species *i*
Y_i	[-]	Mass fraction of species *i*
μ	[kg m^{-1} s^{-1}]	Viscosity
ε	[-]	Electrode porosity
ξ	[-]	Electrode tortuosity
Ω_D	[-]	Dimensionless diffusion collision integral
ρ	[kg m^{-3}]	Density of the gas mixture

References:

[1] M. Granovskii, I. Dincer, M.A. Rosen, I. Pioro, Performance assessment of a combined system to link a supercritical water-cooled nuclear reactor and a thermaochemical water splitting cycle for hydrogen production, Energy Conversion and Management 49(2008) 1873-1881. .

[2] M. Ni, M.K.H. Leung, D.Y.C. Leung, K. Sumathy, A review and recent developments in photocatalytic water-splitting using TiO2 for hydrogen production, Renewable and Sustainable Energy Reviews 11(2007) 401-425.

[3] R. Rivera-Tinoco, C. Mansilla, C. Bouallou, Competitiveness of hydrogen production by high temperature electrolysis: impact of the heat source and identification of key parameters to achieve low production cost, Energy Conversion and Management 51(2010) 2623-2634.

[4] S.J. Yoon, Y. Choi, J. Lee, Hydrogen production from biomass tar by catalytic steam reforming, Energy Conversion and Management 51(2010) 42-47.

[5] J. Xuan, M.K.H. Leung, D.Y.C. Leung, M. Ni, Integrating chemical kinetics with CFD modelling for autothermal reforming of biogas, Int. J. Hydrogen Energy 34(2009) 9076-9086.

[6] J.L. Yuan, X.R. Lv, B. Sunden, D.T. Yue, Analysis of parameter effects on transport phenomena in conjunction with chemical reactions in ducts relevant for methane reformers, Int. J. Hydrogen Energy 32(2007) 3887-3898.

[7] M. Zanfir, A. Gavriilidis, Catalytic combustion assisted methane steam reforming in a catalytic plate reactor, Chem. Eng. Sci. 58(2003) 3947-3960.

[8] J.L. Yuan, F. Ren, B. Sunden, Analysis of chemical-reaction-coupled mass and heat transport phenomena in a methane reformer duct for PEMFCs, Int. J. Heat Mass Transfer 50(2007), 687-701.

[9] T.S. Lee, J.N. Chung, Y.C. Chen, Design and optimization of a combined fuel reforming and solid oxide fuel cell system with anode off-gas recycling, Energy Conversion and Management 52(2011) 3214-3226.

[10] T. Jiang, Q. Zhang, T.J. Wang, Q. Zhang, L.L. Ma, High yield of pentane production by aqueous-phase reforming of xylitol over Ni/HZSM-5 and Ni/MCM22 catalysts, Energy Conversion and Management 59(2012) 58-65.

[11] B.A. Haberman, J.B. Young, Three-dimensional simulation of chemically reacting gas flows in the porous support structure of an integrated-planar solid oxide fuel cell, Int. J. Heat Mass Transfer 47(2004) 3617-3629.

[12] M.W. Chase, NIST-JANAF thermochemical tables. (4^{th} edition) American Chemical Society, American Institute of Physics for the National Institute of Standards and technology (1998).

[13] M. Ni, 2D thermal modeling of a solid oxide electrolyzer cell (SOEC) for syngas production by H_2O/CO_2 co-electrolysis, Int. J. Hydrogen Energy 37(2012) 6389-6399.

[14] C.Y. Wang, Fundamental models for fuel cell engineering, Chem. Rev. 104(2004) 4727-4765.

[15] M. Ni, Thermo-electrochemical modelling of ammonia-fueled solid oxide fuel cells considering ammonia thermal decomposition in the anode, Int. J. Hydrogen Energy 36(2011) 2027-2036.

[16] R.C. Reid, J.M. Prausnitz, B.E. Poling, The properties of gases & liquids (4th edition). McGraw-Hill Book Company, New York (1987).

[17] M. Ni, Modeling of SOFC running on partially pre-reformed gas mixture, Int. J. Hydrogen Energy 37(2012) 1731-1745.

[18] W. Lehnert, J. Meusinger, F. Thom, Modeling of gas transport phenomena in SOFC anodes, Journal of Power Sources 87(2000) 57-63.

[19] I. Drescher, W. Lehnert, J. Meusinger, Structural properties of SOFC anodes and reactivity, Electrochimica Acta 43 (1998) 3059-3068.

List of Tables

List of Figures*

* Note:

All figures are **to be reproduced in color on the Web (free of charge) and in black-and-white in print**

Table 1. Parameters used in calculating the effective diffusion coefficients [16]

	CO	CO_2	H_2	O_2	CH_4	N_2	H_2O
σ_i	3.69	3.941	2.827	3.467	3.758	3.798	2.641
ε_i / k	91.7	195.2	59.7	106.7	148.6	71.4	809.1

Table 2 Parameters used in simulation.

Parameter	Value
Operating temperature, T (K)	1173
Operating pressure, P (bar)	1.0
Porosity of the porous catalyst layer, ε	0.4
Tortuosity of the porous catalyst layer, ξ	3.0
Permeability of the porous catalyst layer, B_g , (m^2)	2×10^{-10}
Average pore radius, r_p (μm)	1.0
Thickness of the porous catalyst layer (cm)	0.4
Length of the Compact Reformer (cm)	20
Thickness of solid plate (cm)	0.1
Inlet velocity at the reforming duct: U_0 ($m.s^{-1}$)	3.0
Height of the reforming duct (cm)	0.4

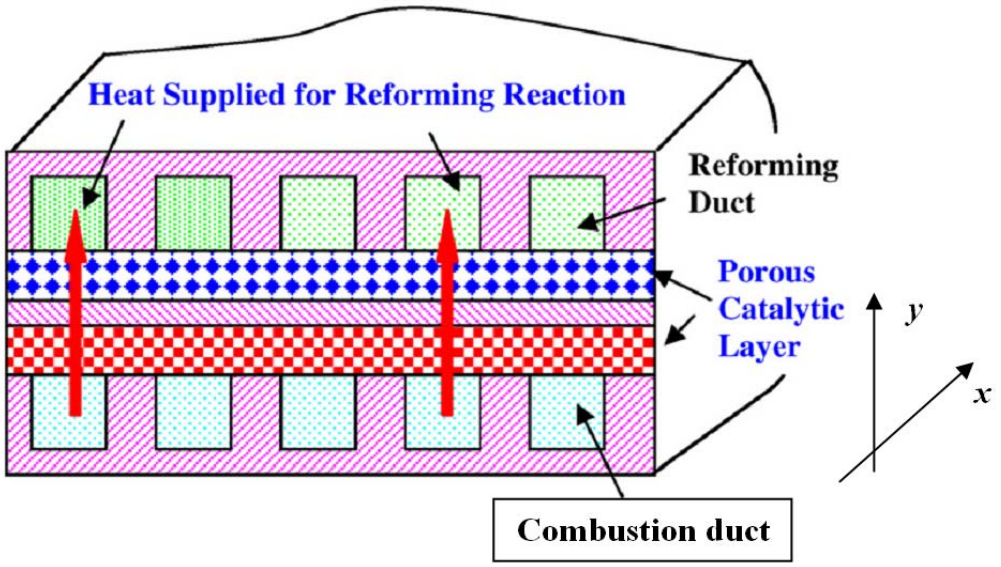

Figure 1.

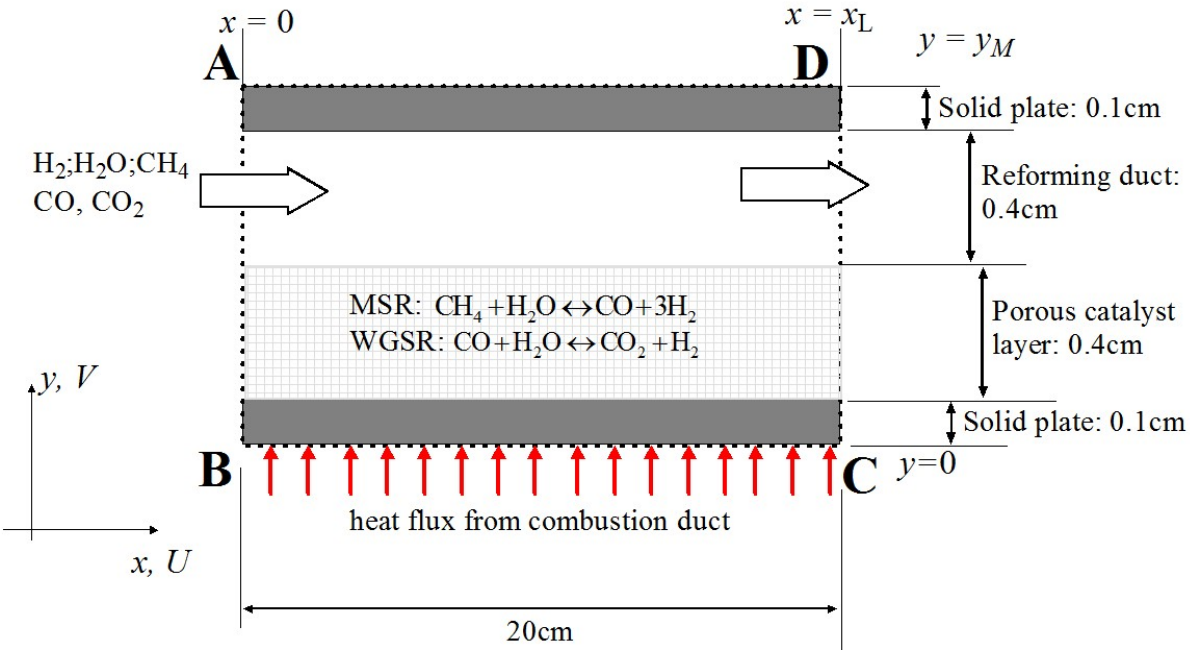

Figure 2

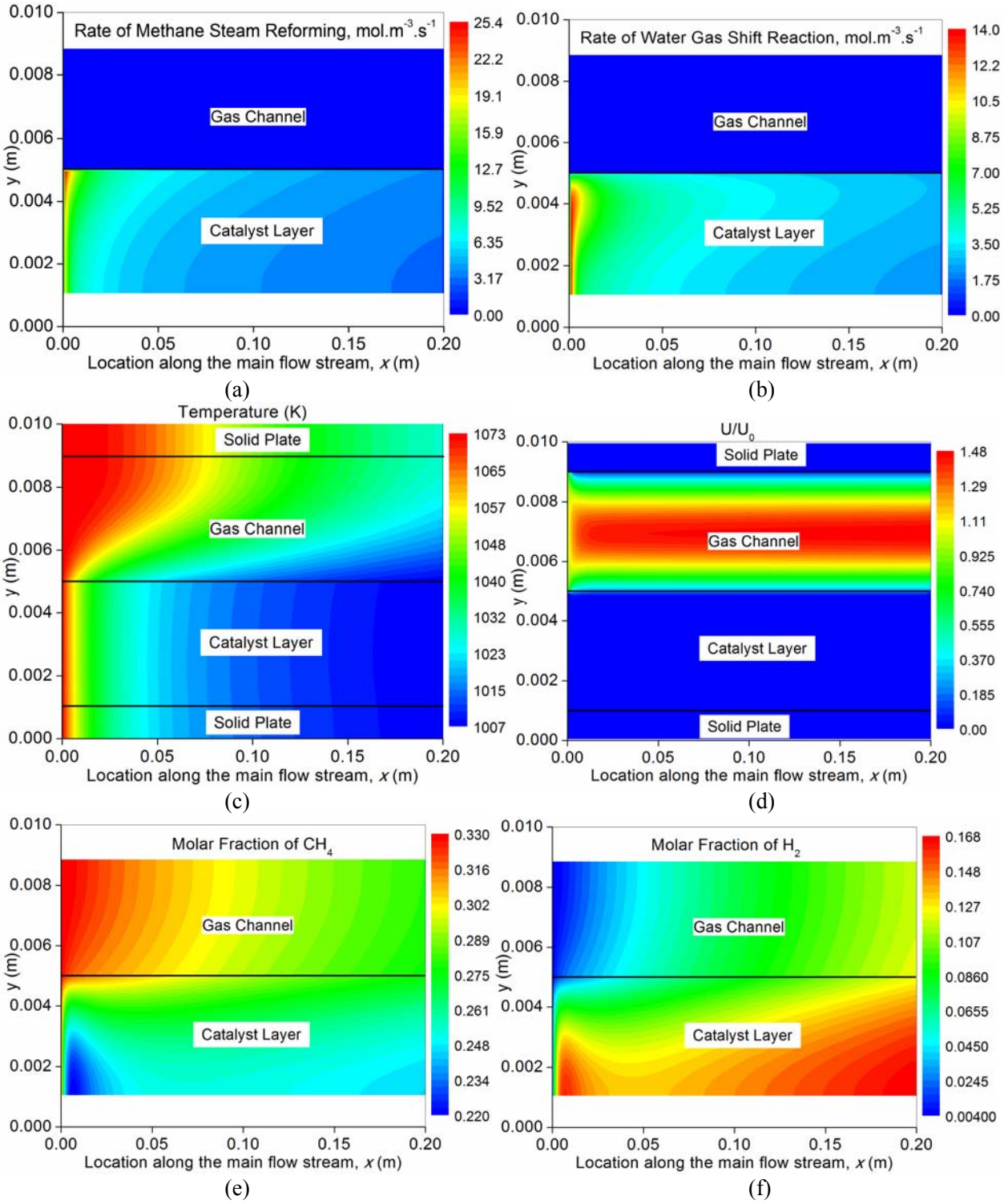
Rate of Methane Steam Reforming, mol.m-3.s-1
Gas Channel
Catalyst Layer
y (m)
Location along the main flow stream, x (m)
(a)
Rate of Water Gas Shift Reaction, mol.m-3.s-1
Gas Channel
Catalyst Layer
y (m)
Location along the main flow stream, x (m)
(b)
Temperature (K)
Solid Plate
Gas Channel
Catalyst Layer
Solid Plate
y (m)
Location along the main flow stream, x (m)
(c)
U/U0
Solid Plate
Gas Channel
Catalyst Layer
Solid Plate
y (m)
Location along the main flow stream, x (m)
(d)
Molar Fraction of CH4
Gas Channel
Catalyst Layer
y (m)
Location along the main flow stream, x (m)
(e)
Molar Fraction of H2
Gas Channel
Catalyst Layer
y (m)
Location along the main flow stream, x (m)
(f)

Figure 3.

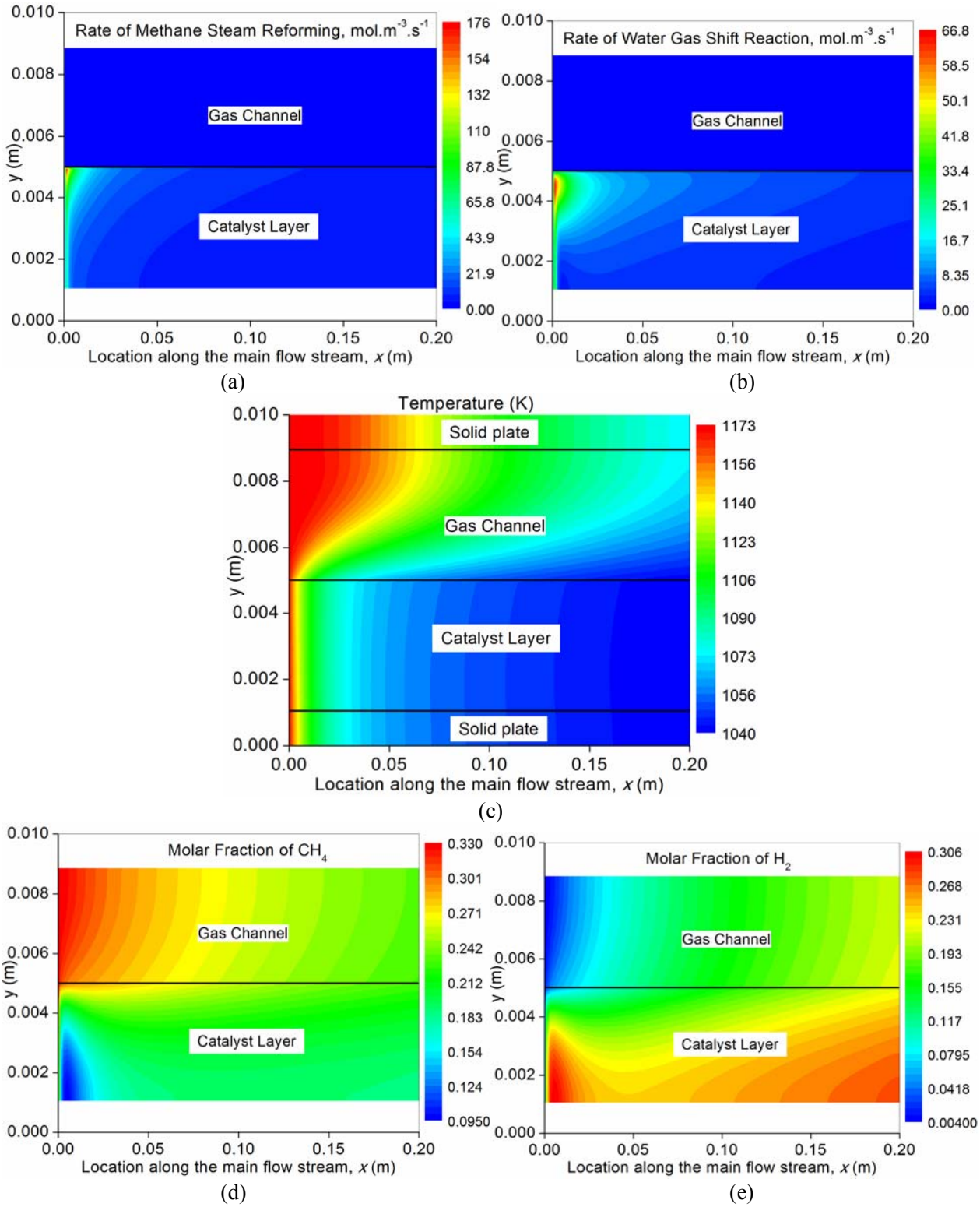
Rate of Methane Steam Reforming, mol.m-3.s-1
Gas Channel
Catalyst Layer
y (m)
Location along the main flow stream, x (m)
(a)
Rate of Water Gas Shift Reaction, mol.m-3.s-1
Gas Channel
Catalyst Layer
y (m)
Location along the main flow stream, x (m)
(b)
Temperature (K)
Solid plate
Gas Channel
Catalyst Layer
Solid plate
y (m)
Location along the main flow stream, x (m)
(c)
Molar Fraction of CH4
Gas Channel
Catalyst Layer
y (m)
Location along the main flow stream, x (m)
(d)
Molar Fraction of H2
Gas Channel
Catalyst Layer
y (m)
Location along the main flow stream, x (m)
(e)

Figure 4.

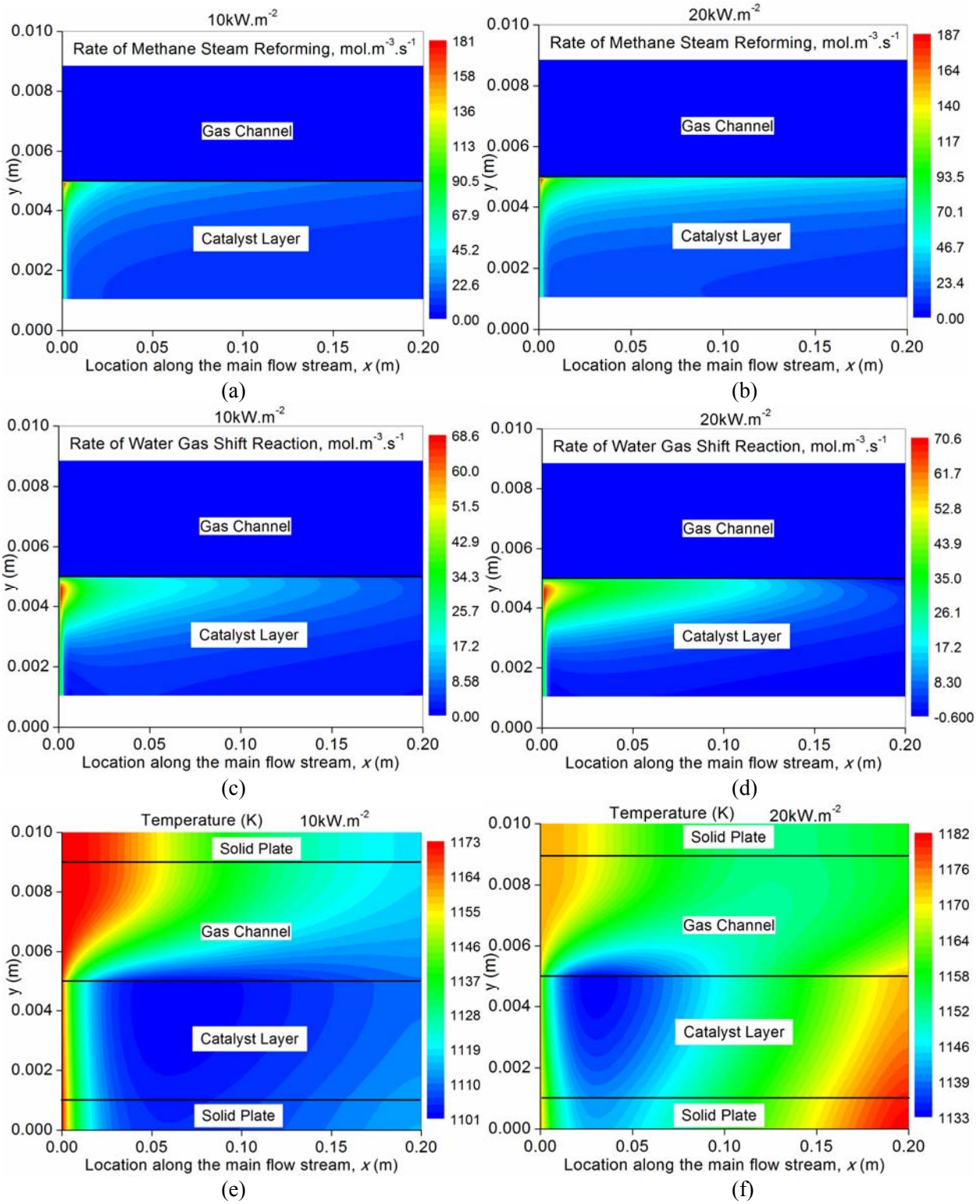
10kW.m-2
Rate of Methane Steam Reforming, mol.m-3.s-1
Gas Channel
Catalyst Layer
y (m)
Location along the main flow stream, x (m)
(a)
20kW.m-2
Rate of Methane Steam Reforming, mol.m-3.s-1
Gas Channel
Catalyst Layer
y (m)
Location along the main flow stream, x (m)
(b)
10kW.m-2
Rate of Water Gas Shift Reaction, mol.m-3.s-1
Gas Channel
Catalyst Layer
y (m)
Location along the main flow stream, x (m)
(c)
20kW.m-2
Rate of Water Gas Shift Reaction, mol.m-3.s-1
Gas Channel
Catalyst Layer
y (m)
Location along the main flow stream, x (m)
(d)
Temperature (K)
10kW.m-2
Solid Plate
Gas Channel
Catalyst Layer
Solid Plate
y (m)
Location along the main flow stream, x (m)
(e)
Temperature (K)
20kW.m-2
Solid Plate
Gas Channel
Catalyst Layer
Solid Plate
y (m)
Location along the main flow stream, x (m)
(f)

Figure 5.

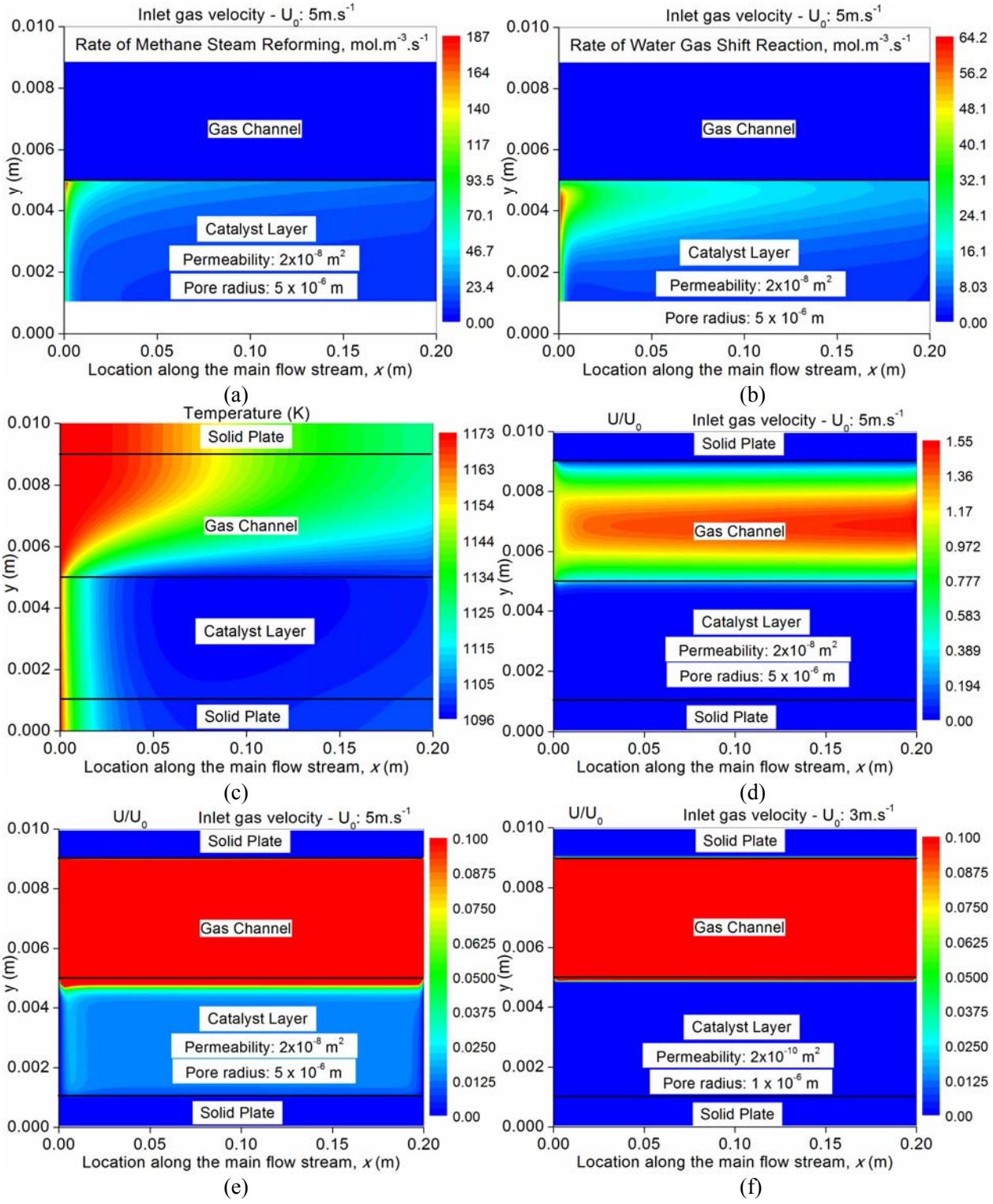
Inlet gas velocity - U0: 5m.s-1
Rate of Methane Steam Reforming, mol.m-3.s-1
Gas Channel
Catalyst Layer
Permeability: 2x10-8 m2
Pore radius: 5 x 10-6 m
y (m)
Location along the main flow stream, x (m)
(a)
Inlet gas velocity - U0: 5m.s-1
Rate of Water Gas Shift Reaction, mol.m-3.s-1
Gas Channel
Catalyst Layer
Permeability: 2x10-8 m2
Pore radius: 5 x 10-6 m
Location along the main flow stream, x (m)
(b)
Temperature (K)
Solid Plate
Gas Channel
Catalyst Layer
Solid Plate
Location along the main flow stream, x (m)
(c)
U/U0
Inlet gas velocity - U0: 5m.s-1
Solid Plate
Gas Channel
Catalyst Layer
Permeability: 2x10-8 m2
Pore radius: 5 x 10-6 m
Solid Plate
Location along the main flow stream, x (m)
(d)
U/U0
Inlet gas velocity - U0: 5m.s-1
Solid Plate
Gas Channel
Catalyst Layer
Permeability: 2x10-8 m2
Pore radius: 5 x 10-6 m
Solid Plate
Location along the main flow stream, x (m)
(e)
U/U0
Inlet gas velocity - U0: 3m.s-1
Solid Plate
Gas Channel
Catalyst Layer
Permeability: 2x10-10 m2
Pore radius: 1 x 10-6 m
Solid Plate
Location along the main flow stream, x (m)
(f)

Figure 6.